Hydrogen on screw dislocation in Fe and W: existence of 3D-compound and exotic segregation profile

F Berthier, N. Longa, J. Creuze, B Legrand

▶ **To cite this version:**

F Berthier, N. Longa, J. Creuze, B Legrand. Hydrogen on screw dislocation in Fe and W: existence of 3D-compound and exotic segregation profile. 2023. hal-04272324

HAL Id: hal-04272324
https://hal.science/hal-04272324v1

Preprint submitted on 6 Nov 2023

HAL is a multi-disciplinary open access archive for the deposit and dissemination of scientific research documents, whether they are published or not. The documents may come from teaching and research institutions in France or abroad, or from public or private research centers.

L'archive ouverte pluridisciplinaire **HAL**, est destinée au dépôt et à la diffusion de documents scientifiques de niveau recherche, publiés ou non, émanant des établissements d'enseignement et de recherche français ou étrangers, des laboratoires publics ou privés.

Hydrogen on screw dislocation in Fe and W:

existence of 3D-compound and exotic segregation profile.

F. Berthier[1*], N. Longa[1], J. Creuze[1], B. Legrand[2]

[1] Université Paris-Saclay, CNRS, UMR 8182, Institut de chimie moléculaire et des matériaux d'Orsay, 91400 Orsay, France

[2]Université Paris-Saclay, CEA, Service de recherche en Corrosion et Comportement des Matériaux, SRMP, 91191, Gif-sur-Yvette, France

*fabienne.berthier@universite-paris-saclay.fr

Key words

Segregation, long-range ordering, short-range ordering, hydrogen, screw dislocation, iron, tungsten

Abstract

We present the study of hydrogen atom segregation on screw dislocation in Fe and W metals by means of rigid lattice Monte Carlo simulations using interaction energies obtained from *ab initio* calculations. These interaction energies are attractive or repulsive depending on direction and distance. This high interaction anisotropy leads to the formation of a 3D compound for both iron and tungsten. A second consequence is that, within a given temperature range, hydrogen enrichment is greater at the outer than at the innermost sites of the dislocation. This unusual behavior is only observed for iron. We propose a mean-field model that accounts for the ordering phenomenon to explain the results and the differences between the two metals.

1. Introduction

The use of hydrogen in energy applications to replace fossil fuels represents a considerable challenge, in particular because hydrogen degrades the mechanical properties of materials. The embrittlement of metallic materials by hydrogen was identified a century ago [1] and is still the subject of intensive studies [2–7]. It is also well known that the repartition of solute atoms, such as hydrogen, near crystallographic defects (point defects, dislocations, surfaces, and interfaces) differs from the bulk one. Experimental studies have shown that the presence of hydrogen on dislocations modifies their mobility [8–13]. Thus, knowledge of the hydrogen chemical composition on a dislocation is fundamental to understand how hydrogen reduces ductility in metals.

Hydrogen segregation has often been studied at vacancy [14], surfaces [15,16], grain boundaries [2,14,17–23], and dislocations [24–30]. For dislocations, hydrogen segregation was modeled either using elastic theory [31,32], Molecular Statics or Monte-Carlo (MC) simulations with semi-empirical potentials [31,33–35], or using *ab initio* calculations to obtain energetic interactions used as input data in rigid-lattice MC simulations or mean-field (MF) models [25,29,30,36,37].

In most cases the segregation is not confined to the dislocation axis and other sites in the vicinity of the dislocation may also be favorable for segregation. Enrichment is generally stronger at sites near the dislocation axis than at outer sites. This may explain why mean-field models rarely consider the sites furthest from the dislocation center. By considering only central sites, segregation at peripheral sites is assumed to be negligible. However, for other defects (surfaces, grain boundaries), studies show that the segregation profile is driven by interactions between adjacent planes [38,39,48,40–47]. What about dislocations? What is the segregation profile from the central to the outermost sites of the dislocation? And what happens when the interactions are anisotropic?

To answer these questions, we investigate the hydrogen segregation at 1/2 <111> screw dislocation in iron and tungsten. *Ab initio* energetic parameters [29] are introduced into Monte Carlo simulations and into a mean-field (MF) modelling which allow the emergence of

order phenomena. These energetic parameters show that many dislocation sites are favorable to hydrogen atom segregation; and that interactions between hydrogen atoms are highly diverse, some of them being characteristic of phase separation and others of ordering. The difference in hydrogen atom interactions of the two metals may lead to different segregation profiles. The strong anisotropy of interactions leads to the formation of a 3D compound for both iron and tungsten. We also show that, over a given temperature range, hydrogen enrichment is greater in the outer than in the inner sites of the dislocation. This unusual behavior is only observed for iron. To illustrate the importance of the coupling between segregation and ordering, and to explain the differences between the two metals, we compare the results with a homogeneous mean-field model which considers that all sites on a given line near the dislocation have the same concentration.

The paper is organized as follows. We present in section 2 the energetic parameters used to compute segregation profiles in Monte Carlo simulations (section 2.2) and in mean-field models (section 2.3). We detail two mean-field models, the heterogeneous MF which considers two types of sites for each line, in order to describe possible ordering and the homogeneous MF. In section 3, we present the iso-concentrations obtained with the heterogeneous MF for iron and tungsten (section 3.1). Monte Carlo profiles and microstructures are then detailed for both metals (section 3.2). Results are discussed and compared with those obtained with homogeneous MF in section 4, in order to highlight the coupling between segregation and ordering. Finally, in section 5 we list the general conclusions.

2. Methods of calculation

2.1 Energetic parameters

The interaction energies used in our simulations were obtained from *ab initio* calculations [29]. The insertion of hydrogen atoms leads to spontaneous reconstruction of the dislocation core, known as the "hard core". Dislocation sites favorable to the insertion of hydrogen atoms are located at the center of the faces of regular trigonal prisms and on adjacent octahedral sites (see *figure 1a*). Hereafter, we'll refer to the central region of prismatic sites as the

dislocation core, and the peripheral sites as octahedral sites. These include the $O^{(4)}$ sites, then the $O^{(10)}$ sites and the $O^{(11)}$ sites, from the center of the dislocation outwards. Beyond these sites, hydrogen atom insertion takes place on tetrahedral sites.

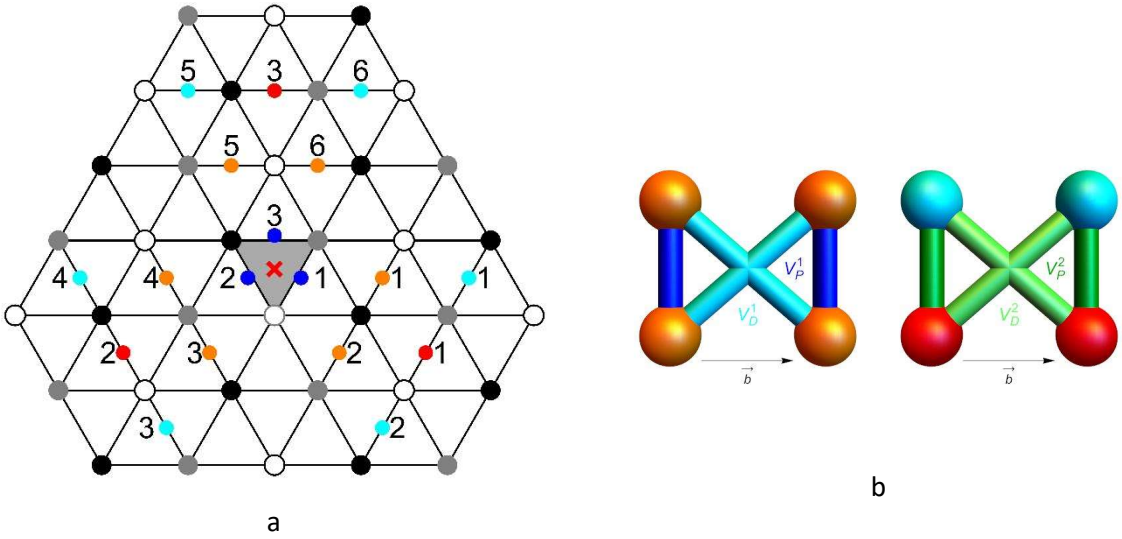

a b

Fig. 1: *Schematic representation of the sites and alloying pair interactions between O sites: (a) projection on the (111) plane, (b) projection along the Burgers vector direction. (a) The metal atoms are represented in white, black and grey according to their original (111) plane in perfect bulk; the reconstructed dislocation core is displayed by a grey triangle and hydrogen atoms are in color: the core sites inside the hard core are depicted blue while the $O^{(4)}$ sites, with k ranging from 1 to 6, are in orange; the $O^{(10)}$ sites, with k ranging from 1 to 3, are in red and the $O^{(11)}$ sites, with k ranging from 1 to 6, are in cyan. (b) Alloying pair interactions between $O^{(4)}$ sites (in blue) and $O^{(10)} - O^{(11)}$ sites (in green).*

To describe the segregation of hydrogen on the dislocation, we use a lattice-gas model consisting of a 3D array of H insertion sites. The grand-canonical formulation of the Hamiltonian is:

$$H = H_0 + \sum_{i=1}^{N_L} \left(\Delta E_i^{seg,0} \sum_{n=1}^{N_S} p_n^i + \frac{1}{2} \sum_j \sum_{n,m(m\neq n)} V_{nm}^{ij} p_n^i \, p_m^j - \mu \sum_{n=1}^{N_S} p_n^i \right), \qquad (1)$$

where H_0 is a constant term, proportional to the energetic cost to transform a dislocation segment from an easy to a hard core. N_L is the number of lines considered for the insertion of hydrogen atoms and N_S the number of interstitial sites on a line. p_n^i is the occupation number that equals 1 if the site n of line i is occupied by an inserted H-atom and 0 otherwise. The Hamiltonian depends on two elements, the segregation energies $\Delta E_i^{seg,0}$ in dilute limit on

a site of the i–line, and the pair interaction energies V_{nm}^{ij} between hydrogen atoms on two sites n and m on the line i and j, μ being the chemical potential.

The segregation energy of H atom in dilute limit is $\Delta E_i^{seg,0} = E_i^{ins} - E_{bulk}^{ins}$. E_i^{ins} (respectively, E_{bulk}^{ins}) is the total energy of the system when one H atom is inserted on a site of the i–line (respectively, a bulk site). A negative value of $\Delta E_i^{seg,0}$ means that the incorporation of hydrogen is favored on line i. *Ab initio* calculations show that the sites of the three core lines corresponding to the face centers of the prisms defined by the hard core and the sites of the octahedral lines $O^{(4)}$ (6 lines), $O^{(10)}$ (3 lines) and $O^{(11)}$ (6 lines), thus $N_L = 18$ lines in all, are favorable for the hydrogen segregation for both iron and tungsten (see *Table 1*) [29]. Beyond these sites, the segregation energy in the dilute limit is negligible. At the dislocation, for both iron and tungsten, the segregation will occur preferentially on the core sites, then on the $O^{(4)}$ sites, then on the $O^{(10)}$ site and finally on the $O^{(11)}$ sites (see *Table 1*).

	$\Delta E_{core}^{seg,0}$ (eV)	$\Delta E_{O^{(4)}}^{seg,0}$ (eV)	$\Delta E_{O^{(10)}}^{seg,0}$ (eV)	$\Delta E_{O^{(11)}}^{seg,0}$ (eV)
Iron	-0.22	-0.19	-0.17	-0.07
Tungsten	-0.75	-0.51	-0.35	-0.17

Table 1: *Segregation energy of H atom in dilute limit at the various dislocation sites* [29].

Whatever the line (core, $O^{(4)}$, $O^{(10)}$ or $O^{(11)}$) and the metal (iron or tungsten), there is no nearest neighbor interaction between H atoms of the same line along the Burgers vector direction (intra-line interaction), nor any interaction between H atoms in core lines and H atoms of $O^{(4)}$ lines, or between the H atoms of $O^{(4)}$ lines and the H atoms of $O^{(10)}$ and H atoms of $O^{(11)}$ lines. *Ab initio* calculations show (see *Table 2*) that perpendicular inter-line interactions are negative between two atoms in nearest neighbor positions located in the same plane (111) (see *figure 1b*), both for two atoms in the $O^{(4)}$ lines, V_P^1, and for two atoms in the $O^{(10)}$ and $O^{(11)}$ lines, V_P^2. Diagonal inter-line interactions, *i.e.* between two atoms in two successive (111) planes, are positive, both for atoms in the $O^{(4)}$ lines, V_D^1, and for atoms in the $O^{(10)}$ and $O^{(11)}$ lines, V_D^2. Let us recall that a negative (respectively positive) value indicates that the interaction is attractive (resp. repulsive). Interactions attractive are responsible of phase separation whereas repulsive interactions lead to ordered structures. Therefore, the competition between attractive perpendicular interactions and repulsive

diagonal interactions may lead to ordered structures and simulations are required to take this complexity into account.

	V_P^1 (eV)	V_D^1 (eV)	V_P^2 (eV)	V_D^2 (eV)	V_{eff}^1(eV)	V_{eff}^2(eV)
Iron	-0.25	0.24	-0.17	0.16	0.23	0.15
Tungsten	-0.46	0.41	-0.48	0.24	0.36	0

Table 2: *Interaction energies at the various dislocation sites* [29] *and effective interaction energies* $V_{eff}^i = V_P^i + 2V_D^i$ *with* $i = 1,2$. *All other interaction energies are negligible*.

Note that the energetic parameters for iron and tungsten are very similar, both for segregation energies in the dilute limit and for interaction energies. On average, all tungsten quantities are about twice those of iron. For both metals, $|V_P^1| \approx V_D^1$. For iron $|V_P^2| \approx V_D^2$ but not for tungsten for which $|V_P^2| = 2V_D^2$.

We briefly recall in the following subsections the two methods used to obtain the distribution of hydrogen atoms on the dislocation: the MC simulations and the MF approximation.

2.2 Monte Carlo simulations

To determine the distribution of H atoms onto the different sites of the dislocation, we perform Monte Carlo simulations in the grand-canonical ensemble [49–51], where the bulk concentration of H is determined by the chemical potential μ which is calculated from the mean-field formalism in dilute limit:

$$\mu = E_0 + k_B T \ln \frac{c_{bulk}}{1-c_{bulk}} \ , \qquad (2)$$

where E_0 is the incorporation energy of one isolated hydrogen atom into a bulk tetrahedral site and c_{bulk} the bulk concentration of hydrogen. In these simulations, we do not equilibrate the bulk, but only consider the insertion of hydrogen atoms at the dislocation sites at a given μ value. We could also consider an infinite simulation box to equilibrate the bulk for the same value of chemical potential. For very dilute solutions (less than 1000 appm), interactions between hydrogen atoms in the bulk are negligible, and MC simulations would give the same bulk concentration as the mean-field approximation (eq. 2). We therefore consider the behavior of an isolated dislocation in an infinite box. Since the dislocation density is zero, the

nominal concentration (the number of hydrogen atoms per metal atom) is simply $c_{nom} = 6\, c_{bulk}$ [29].

MC simulations in the grand canonical ensemble enables the optimization of both the number and the distribution of the hydrogen atoms on the different sites. Only incorporation and extraction of hydrogen atoms are proposed. A site is chosen randomly. If the site is empty then the incorporation of a hydrogen atom is proposed, otherwise extraction is proposed. A trial is accepted/rejected following the Metropolis algorithm [52]. The probabilities of incorporation and extraction are respectively:

$$P_I = \frac{N}{N_H+1}\exp\left(-\frac{\Delta E_I}{k_B T}\right) \text{ and } P_E = \frac{N_H}{N}\exp\left(-\frac{\Delta E_E}{k_B T}\right), \quad (3)$$

with N the total number of sites ($N = N_L \times N_S$) and N_H the number of hydrogen atoms in the cell. ΔE_I (respectively ΔE_E) represents the energy variation due to the incorporation (resp. extraction) of a hydrogen atom. Each energy is given by the Hamiltonian (eq. 1) which depends on the configuration via the site occupation numbers. Therefore, MC simulations allow one the determination of iso-concentrations and isotherms, *i.e.* the evolution of the H-concentration for the dislocation sites as a function of the temperature for a fixed value of the chemical potential (or of the bulk concentration) and respectively as a function of the chemical potential at a given temperature.

We perform the simulations for a 3D-lattice containing N_L lines and assuming periodic boundary conditions. Each line is composed of $N_S = 100$ sites. The total number of sites is $N = 1800$ and the number of MC steps (number of incorporation/extraction events) is $N_{MC} = 10^6$.

2.3 Mean-Field modelling

Starting from the Ising Hamiltonian, we can define different models using the mean-field approximation to predict segregation. First, to describe an ordered structure, we considered a model in which we introduced sub-lattices for each line near the dislocation. Then, we assume that each line has a homogeneous distribution as in [29]. In the following we will refer to these models as heterogeneous or homogeneous, respectively.

Minimizing the grand-canonical free energy with respect to the concentrations c_X (where X is a line or a sub-lattice on a line) leads to the segregation isotherm at temperature T

$$\frac{c_X}{1-c_X} = \frac{c_{bulk}}{1-c_{bulk}} exp\left(-\frac{\Delta E_X^{seg}}{k_B T}\right), \quad (4)$$

with c_{bulk} the bulk concentration (given by eq. 2), k_B the Boltzmann constant and ΔE_X^{seg} the enthalpy of segregation which will be detailed below for each object considered (line or sub-lattice per line).

2.3.1 Heterogeneous Mean-Field

Given the values of the interaction energies used in the Ising model (*Table 2*), we can expect, in the ground state, an alternation of every second site occupied by a hydrogen atom in the direction of the Burgers vector. The sites are occupied simultaneously on neighboring octahedral lines in the direction perpendicular to the Burgers vector (see *figure 2*).

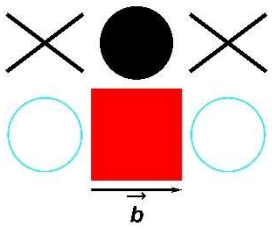

Fig. 2: *Schematic representation of the local arrangement of H-atoms on a pair of neighboring $O^{(4)}$ lines or $O^{(10)}$ and $O^{(11)}$ lines in the ground state (projection along the Burgers vector direction). Once a first hydrogen atom is placed on a line (red square), the most favorable site to insert a second hydrogen atom is the neighboring site of the second line (black disk) and the less favorable sites are the neighboring sites in diagonal (crosses).*

For a concentration equal to ½, this scheme is repeated along the Burgers vector direction. The system being heterogeneous with plain and empty sites, it is necessary to introduce sub-lattices (denoted α and β in the following), such that one (α) describes the set of occupied sites and the other one (β) the set of empty sites. This model then enables us to study the evolution of an ordered state as a function of temperature, by determining the concentration for each sub-lattice.

The system is then described by 7 equations, one for the core, and 6 for the octahedral lines (3 for the α sub-lattices and 3 for the β sub-lattices). The segregation enthalpies of each sub-lattice of the octahedral lines are defined as follows:

$$\begin{cases} \Delta E^{seg}_{O^{(4)}_\alpha} = \Delta E^{seg,0}_{O^{(4)}} + \left(V_P^1\, c_{O^{(4)}_\alpha} + 2V_D^1\, c_{O^{(4)}_\beta}\right) \\ \Delta E^{seg}_{O^{(4)}_\beta} = \Delta E^{seg,0}_{O^{(4)}} + \left(V_P^1\, c_{O^{(4)}_\beta} + 2V_D^1\, c_{O^{(4)}_\alpha}\right) \\ \Delta E^{seg}_{O^{(10)}_\alpha} = \Delta E^{seg,0}_{O^{(10)}} + 2\left(V_P^2\, c_{O^{(11)}_\alpha} + 2V_D^2\, c_{O^{(11)}_\beta}\right) \\ \Delta E^{seg}_{O^{(10)}_\beta} = \Delta E^{seg,0}_{O^{(10)}} + 2\left(V_P^2\, c_{O^{(11)}_\beta} + 2V_D^2\, c_{O^{(11)}_\alpha}\right) \\ \Delta E^{seg}_{O^{(11)}_\alpha} = \Delta E^{seg,0}_{O^{(11)}} + \left(V_P^2\, c_{O^{(10)}_\alpha} + 2V_D^2\, c_{O^{(10)}_\beta}\right) \\ \Delta E^{seg}_{O^{(11)}_\beta} = \Delta E^{seg,0}_{O^{(11)}} + \left(V_P^2\, c_{O^{(10)}_\beta} + 2V_D^2\, c_{O^{(10)}_\alpha}\right) \end{cases} \quad (5)$$

This model includes the attractive interactions for the same sub-lattice (α or β) as well as the repulsive interactions between the two sub-lattices α and β. The concentration of a line is equal to the average of the sub-lattice concentrations: $c_{O^{(x)}} = \left(c_{O^{(x)}_\alpha} + c_{O^{(x)}_\beta}\right)/2$, with $x = 4$, 10 or 11.

Numerical resolution of equations (4) at a given temperature yields isotherms, i.e. concentrations c_X as a function of c_{bulk}. Iso-concentrations are obtained for a fixed nominal concentration c_{nom}.

2.3.2 Homogeneous Mean-Field

The simplest model assumes that there is no local order on a line, in which case all the sites of a line are equivalent and the concentration is uniform throughout the line. Then, the system is described by 4 equations which lead to the concentrations of the core lines, and of the octahedral lines $O^{(4)}$, $O^{(10)}$ and $O^{(11)}$. The segregation enthalpies of each line are defined as follows:

$$\begin{cases} \Delta E_{core}^{seg} = \Delta E_{core}^{seg,0}, \\ \Delta E_{O^{(4)}}^{seg} = \Delta E_{O^{(4)}}^{seg,0} + V_{eff}^{1}\, c_{O^{(4)}}, \\ \Delta E_{O^{(10)}}^{seg} = \Delta E_{O^{(10)}}^{seg,0} + 2V_{eff}^{2}\, c_{O^{(11)}}, \\ \Delta E_{O^{(11)}}^{seg} = \Delta E_{O^{(11)}}^{seg,0} + V_{eff}^{2}\, c_{O^{(10)}}, \end{cases} \quad (6)$$

where $V_{eff}^{1} = V_{P}^{1} + 2V_{D}^{1}$ and $V_{eff}^{2} = V_{P}^{2} + 2V_{D}^{2}$ are effective interactions between $O^{(4)}$ sites and between $O^{(10)}$ and $O^{(11)}$ sites. The values in *Table 2* give $V_{eff}^{1} = 0.23$ eV and $V_{eff}^{2} = 0.15$ eV for iron and $V_{eff}^{1} = 0.36$ eV and $V_{eff}^{2} = 0$ eV for tungsten. Indeed, all these interactions are positive or null, and we can already observe that for tungsten, only the $O^{(4)}$ line has non-zero interactions. The consequences of having only positive interactions will be studied later.

3. Results

3.1 Heterogeneous mean field

We use the heterogeneous model described in section 2.3.1 to predict the evolution of the concentration of each line and of the sub-lattice concentrations as a function of temperature. For iron, the iso-concentrations for $c_{nom} = 100$ appm have the following features (see *Figure 3*):

- At low temperatures the iso-concentrations are characterized by two plateaus with a greater segregation in the core line than in the octahedral lines. The core sites are saturated ($c_{core} = 1$) by hydrogen atoms, while the octahedral lines, $O^{(4)}$, $O^{(10)}$ and $O^{(11)}$, have a concentration equal to ½ (see *figure 3a*). For each octahedral line, the α sub-lattice is saturated, while the concentration of the β sub-lattice is zero (see *figure 3b*). This is the signature of an ordered structure.
- As usual, when T increases, after the plateaus, concentrations decrease. Concentrations of the core line, and of the octahedral lines, $O^{(10)}$and $O^{(11)}$ decrease at a lower temperature than the $O^{(4)}$ line concentration. This result is surprising, as one might think that enrichment follows the hierarchy of segregation energies in the dilute limit, and therefore that the inner lines are richer than the peripheral lines. To quantify the inversion of enrichment, we define a decay temperature $T_{1/2}$ for each line as the temperature at which the line concentration is half the concentration at

0 K, *i.e.* the temperature at which $c_{core} = 0.5$ for the core line and $c_{O^{(X)}} = 0.25$ for the octahedral lines. The hierarchy of the decay temperatures is the following: $T_{1/2}^{O^{(11)}} = T_{1/2}^{O^{(10)}} \approx T_{1/2}^{core} < T_{1/2}^{O^{(4)}}$. Hence, between $T_{1/2}^{core} = 349$ K and $T_{1/2}^{O^{(4)}} = 354$ K, hydrogen enrichment is greater at the $O^{(4)}$ sites than at the core sites.

- For the core lines, the decrease is monotonic whereas for the octahedral lines, the iso-concentrations are van der Waals loops both for average concentrations (see *figure 3a*) and α sub-lattice concentrations (see *figure 3b*). This is the signature of phase separation transitions that are due to the attractive perpendicular inter-line interactions V_P^1 and V_P^2 (between 2 atoms of 2 adjacent lines in the same (111) plane).
- The $O^{(10)}$ and $O^{(11)}$ lines are coupled, their characteristic temperatures are identical. The presence of a multilayer phase transition of first order affecting lines $O^{(10)}$ and $O^{(11)}$ differs strongly from the $O^{(4)}$line, for which a monolayer phase transitions is observed [43].

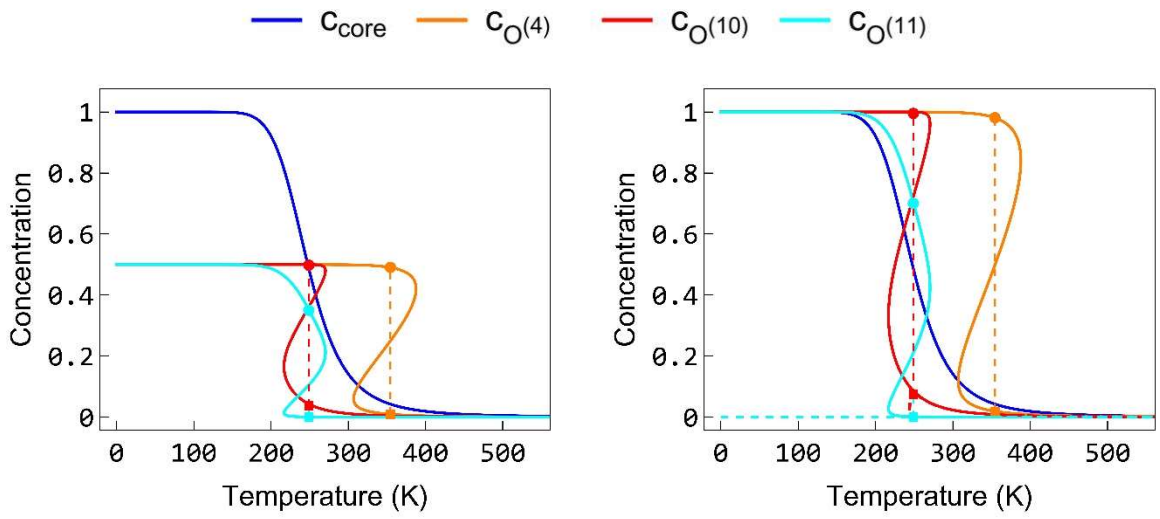

Fig. 3: *Heterogeneous Mean-Field iso-concentrations in iron. Evolution with temperature of lines concentrations (a) and of sub-lattice concentrations (b) for* $c_{nom} = 100$ *appm. (b) Sub-lattices* α *(hydrogen-rich): solid lines, sub-lattices* β *(hydrogen-poor): dashed lines. All the thermodynamic states are represented (stable, metastable, and unstable). Vertical dashed lines (in red and in orange) indicate*

the $T_{1/2}$ *decay temperatures of the* $O^{(10)}$, $O^{(11)}$ *and* $O^{(4)}$ *lines. Dots and squares represent states having the same free energy.*

Note that Van der Waals loops characterize all states around $T_{1/2}$, stable, metastable and unstable. If we consider only the most stable states for each temperature, the octahedral curves become discontinuous at the decay temperature (see *Figure 4*). With increasing temperature, the phase separation leads to a sudden drop of the α sub-lattice concentrations of the octahedral lines from hydrogen-rich to hydrogen-poor states, both states having the same free energy at the transition temperature.

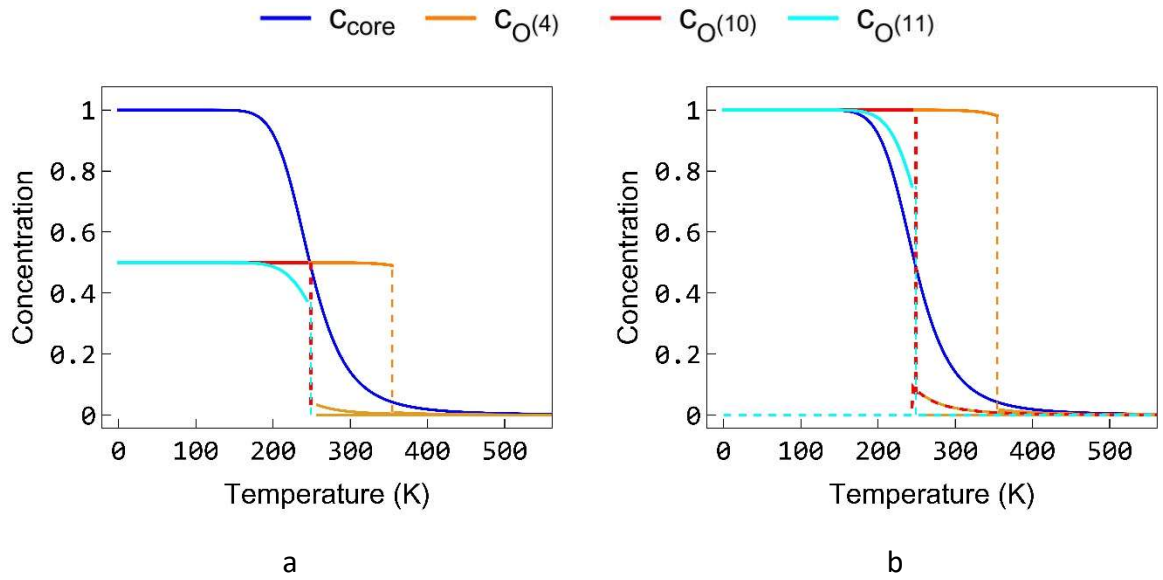

a b

Fig. 4: *Heterogeneous Mean-Field iso-concentrations in iron. Only stable states are represented. Evolution with temperature of lines concentrations (a) and of sub-lattice concentrations (b) for* $c_{nom} = 100$ *appm. (b) Sub-lattices* α *(hydrogen-rich): solid lines, sub-lattices* β *(hydrogen-poor): dashed lines.*

Almost all these characteristics are also observed on iso-concentrations for tungsten (see *figure 5*). The main differences are that

- the length of the plateaus at low temperatures goes up to approximately 600 K instead of 200 K for iron,
- the enrichment is always higher in core line than in octahedral lines. This is characterized by the decay temperatures $T_{1/2}$ which follows the order $T_{1/2}^{O^{(11)}} =$

$T_{1/2}^{O^{(10)}} < T_{1/2}^{O^{(4)}} \lesssim T_{1/2}^{core}$. The decay temperatures of the $O^{(4)}$ line and of the core line are almost identical and much higher than the ones of the $O^{(10)}$ and $O^{(11)}$ lines.

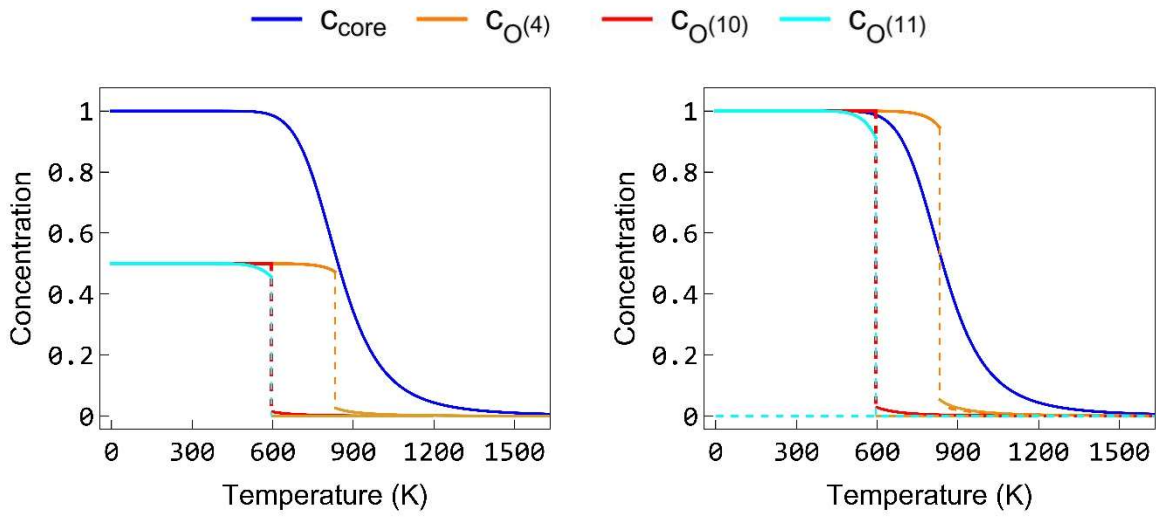

a b

Fig. 5: *Heterogeneous Mean-Field iso-concentrations in tunsten. Only stable states are represented. Evolution with temperature of lines concentrations (a) and of sub-lattice concentrations (b) for* $c_{nom} = 100$ *appm. (b) Sub-lattices* α *(hydrogen-rich): solid lines, sub-lattices* β *(hydrogen-poor): dashed lines.*

Let us analyze the decay temperatures derived from the heterogeneous model for the two metals. The transition of a line X between $c_X = 1$ and $c_X = 0$ occurs at the decay temperature $T_{1/2}^X$ given by

$$T_{1/2}^X = \Delta E_X^{seg}(c_X = 1/2)/k_B ln\left(\frac{c_{bulk}}{1-c_{bulk}}\right). \quad (7)$$

This means that the decay temperatures are driven by the segregation enthalpy value. Therefore, it is instructive to extract this quantity from the energetic values to determine the hierarchical order of the decay temperatures. The more negative $\Delta E_X^{seg}(c_X = 1/2)$, the higher the decay temperature. When the line X is independent, with no intra- and inter-line interactions, such as the core line (for both metals), $\Delta E_X^{seg}(c_X = 1/2) = \Delta E_X^{seg,0}$. The decay temperature of the $O^{(4)}$ line is set by the decrease of the α sub-lattice so it is proportional to $\Delta E_{O^{(4)}}^{seg,0} + V_P^1/2$ for $c_{O_\alpha^{(4)}} = 1/2$ and $c_{O_\beta^{(4)}} = 0$. Since V_p^1 is negative for both metals, the segregation enthalpy $\Delta E_{O^{(4)}}^{seg}$ at the transition is more negative than $\Delta E_{O^{(4)}}^{seg,0}$. For iron, the values resulting from this analysis are -0.22 eV for the core line and -0.315 eV for the $O^{(4)}$

line. The segregation occurs thus preferentially on the α sub-lattice of the $O^{(4)}$ line. For tungsten, the values are respectively -0.75 eV and -0.74 eV for the core and the $O^{(4)}$ line. The two values are very close; the segregation is slightly favorable on the core line. At the transition of the α sub-lattice of line $O^{(10)}$ (respectively $O^{(11)}$) we can assume that $c_{O_\alpha^{(11)}} = 0 = c_{O_\beta^{(11)}}$ (resp. $c_{O_\alpha^{(10)}} = 0.5, c_{O_\beta^{(10)}} = 0$), leading to very similar segregation enthalpy values for the two lines: $\Delta E^{seg}_{O^{(10)}} = -0.17$ eV (respectively -0.35 eV) and $\Delta E^{seg}_{O^{(11)}} = -0.15$ eV (resp. -0.41 eV) for iron (resp. for tungsten).

In order to illustrate change in enrichment between iron and tungsten, we display the segregation profiles at a low temperature below $T_{1/2}^{O^{(10)}-O^{(11)}}$, at a temperature between $T_{1/2}^{O^{(10)}-O^{(11)}}$ and $T_{1/2}^{O^{(4)}}$, and a high temperature greater than $T_{1/2}^{O^{(4)}}$ (see *figure 6*).

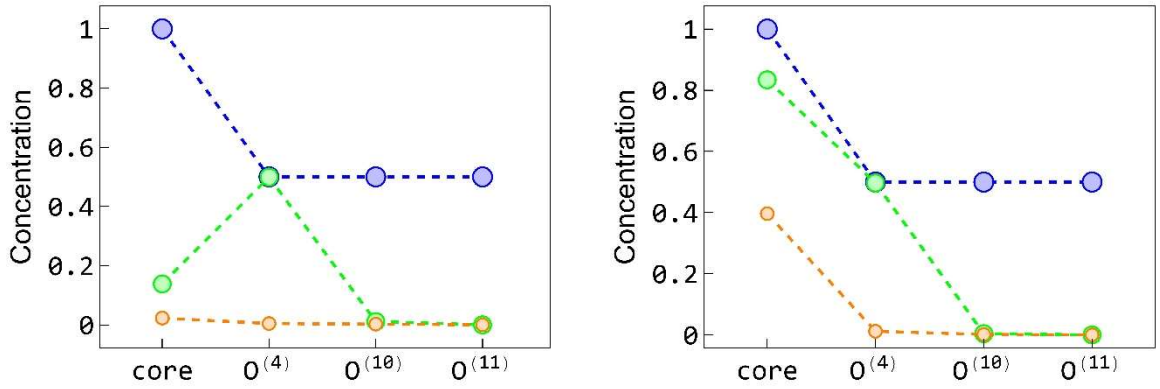

a b

Fig. 6: *Heterogeneous Mean-Field segregation profiles in iron (a) and in tungsten (b) at* $\mathrm{T} = 124$ *K (blue),* $\mathrm{T} = 300$ *K* (*green*) and $T = 388$ *K* (*orange*) *for iron and at* $\mathrm{T} = 104$ *K (blue),* $\mathrm{T} = 728$ *K (green) and* $T = 878$ *K (orange) for tungsten.*

In the case of surface segregation, for systems with a tendency to phase separation (or ordering), the concentration profile is monotonic (or oscillating) as a function of distance from the surface plane [53,54]. The interactions in this case are both attractive and repulsive, so it is not possible to predict the type of profile. The segregation profiles show that, at low temperatures, hydrogen enrichment decreases away from the dislocation center and becomes c_{bulk} beyond the $O^{(11)}$ sites. For temperatures between $T_{1/2}^{O^{(10)}-O^{(11)}}$ and $T_{1/2}^{O^{(4)}}$, the

profile is oscillating for iron, whereas it decreases monotonically for tungsten. For temperatures above $T_{1/2}^{O^{(4)}}$, the profile decreases from the center outwards for both metals, although it is very flat for iron.

The anisotropy of interaction energies leads to both a phase separation transition and an ordering transition, whose properties are determined by isotherms and phase diagrams (see Appendix A).

Let us conclude this section with two comments on these findings. Firstly, an iso-concentration is representative of all the same lines of the dislocation in the mean-field model. For example, the $O^{(4)}$ iso-concentration represents the six $O^{(4)}$ lines. At the decay temperature $T_{1/2}^{O^{(4)}}$, two states have the same free energy. Therefore, it should be asked whether this equilibrium is characterized by a phase separation on each pair of $O^{(4)}$ lines or by a mixture of pair of $O^{(4)}$ lines with one hydrogen-rich pair and two hydrogen-poor pairs, or vice versa. In the case of nanoparticles, for substitutional alloys, the coexistence of two states with the same free energy gives rise to a dynamic equilibrium in phase space affecting the set of facets with the same orientation between two configurations in semi-grand canonical Monte Carlo simulations [55]. The fluctuations of each facet may or may not be correlated, depending on the case. The same question arises for lines $O^{(10)} - O^{(11)}$. Secondly, since there is no phase transition at 1D [56], the question is whether the observed transitions are a peculiarity of the mean-field model, or whether the pairs of $O^{(4)}$ lines and the triplets of $O^{(10)} - O^{(11)}$ lines can be considered as a two-dimensional lattice.

3.2 Monte Carlo simulations

Beyond the mean-field approximation framework, we shall now check the assumption of heterogeneous concentrations in the different lines of sites. We therefore perform Monte Carlo simulations in the grand canonical ensemble with the same Hamiltonian (see section 2.2). MC iso-concentrations are averaged over all sites of the same type of lines once the equilibrium is reached. The agreement between the two methods is satisfactory for both metals (see *figure 7*). MC simulations confirm the presence of plateaus at low temperatures. Hydrogen enrichment forms an ordered structure on the octahedral lines, characterized by an equiatomic composition. The same hierarchical order of the decay transitions is obtained in

MC simulations. Thus, for iron and at low temperatures, the core of the dislocation is richer than the octahedral lines, and at higher temperatures, between $T_{1/2}^{core}$ and $T_{1/2}^{O^{(4)}}$, the $O^{(4)}$ line is richer than the core and the $O^{(10)} - O^{(11)}$ lines. For tungsten, the core lines remain richer than all other lines whatever the temperature. Finally, the$O^{(10)}$ and $O^{(11)}$ lines are coupled as in the mean-field modelling.

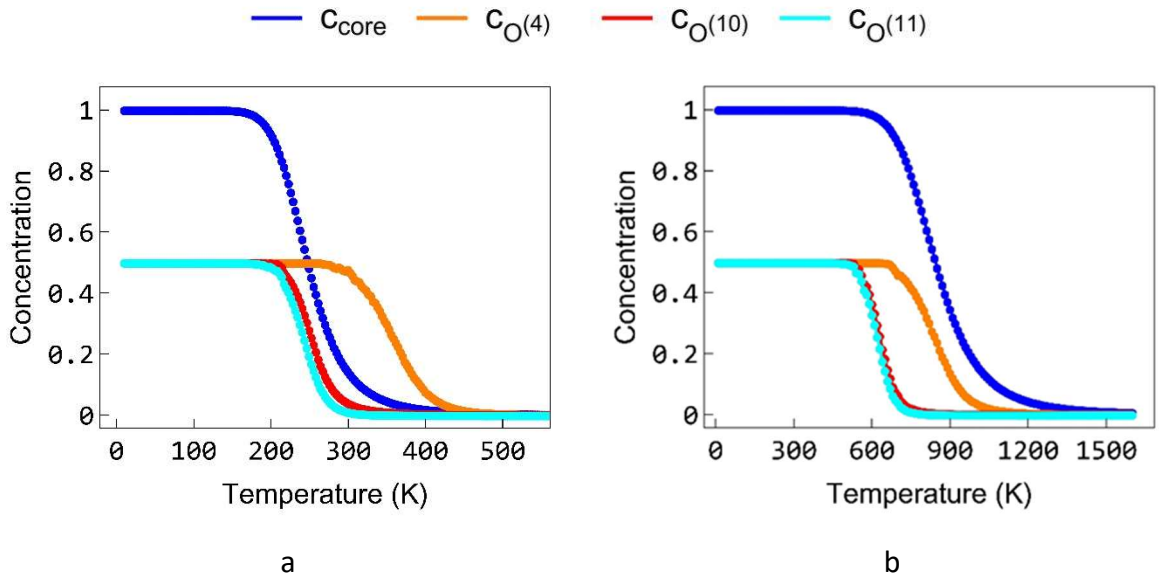

Fig. 7: *Monte Carlo Iso-concentrations in iron (a) and tungsten (b) for* $c_{nom} = 100$ *appm.*

The only difference between the two statistical methods is that the concentrations of the octahedral lines decrease continuously and monotonically. We have also checked that the iso-concentration of each line is identical to the average iso-concentration and does not fluctuate between hydrogen-rich and hydrogen-poor configurations. This suggests that there is no phase separation in MC simulations.

We present the microstructures obtained by Monte Carlo simulations at different temperatures for the two metals. Only one sector (due to the symmetry) of the dislocation is shown, consisting of core line 1, $O^{(4)}$ lines 1 and 2, $O^{(10)}$ line 1 and $O^{(11)}$ lines 1 and 2 (see *figure 1*). Recall that the core lines are independent, that $O^{(4)}$ lines are grouped two by two and each pair is independent, and that each $O^{(10)}$ line is linked to two $O^{(11)}$ lines, each triplet being independent of the other triplets.

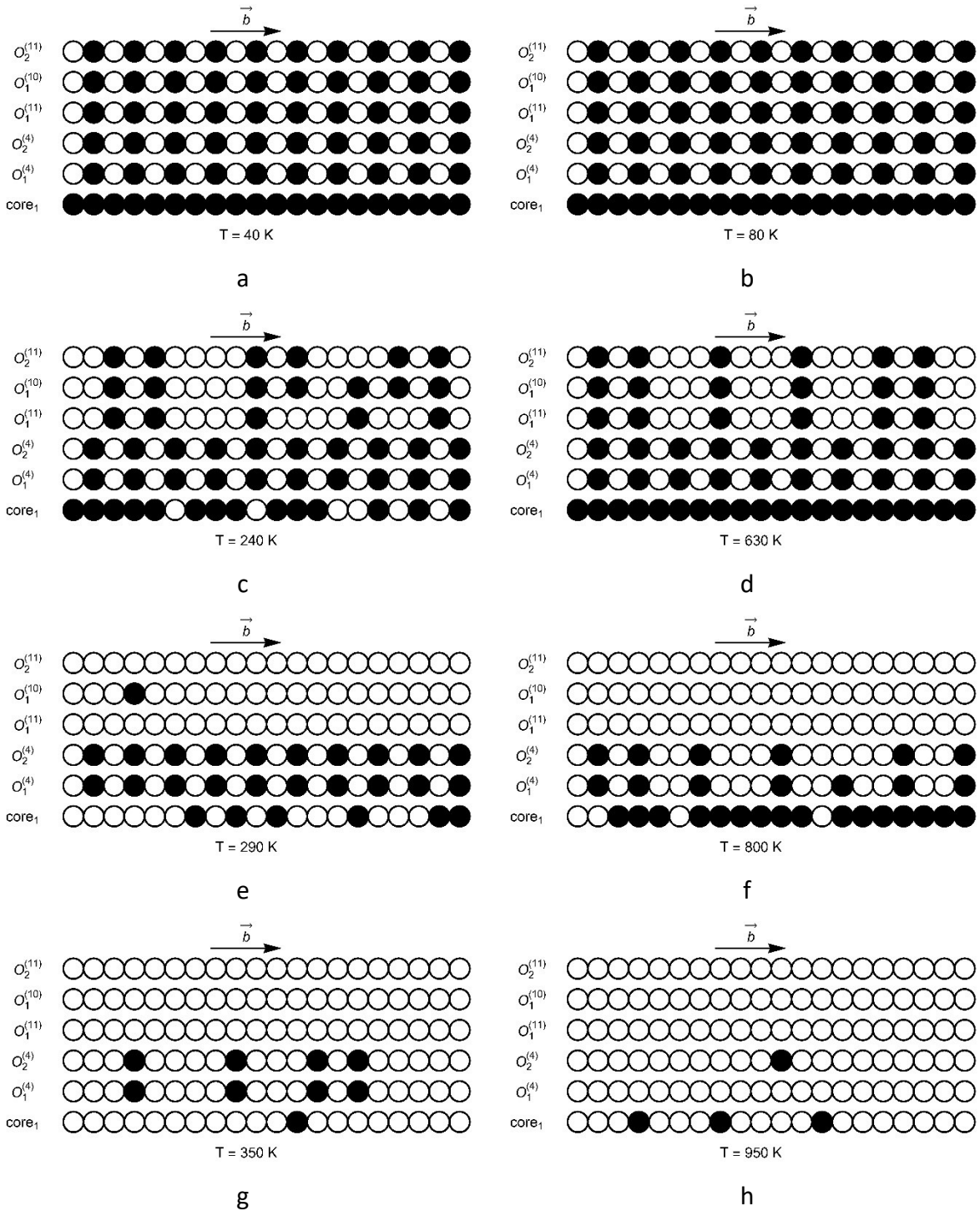

Fig. 8: *Schematic representation of Monte Carlo microstructures along the Burgers vector direction for iron (left column) and tungsten (right column) for* $c_{nom} = 100$ *appm. Circles: empty sites, black disks: hydrogen atoms. Only one part of the dislocation is shown with one core line, one* $O^{(4)}$ *pair and one* $O^{(11)} - O^{(10)} - O^{(11)}$ *triplet. Left column:* $T = 40\ K$ (a), $240\ K$ (c), $290\ K$ (e), $350\ K$ (g), *right column:* $T = 80\ K$ (b), $630\ K$ (d), $800\ K$ (f), $950\ K$ (h).

For both metals, at low temperatures (see *figure 8 a and b*), the core line is saturated with H atoms, while only half of the sites are occupied on the octahedral lines forming an ordered

structure. This explains why the average concentration of octahedral lines is 0.5 (see *figure 7*). Each $O^{(4)}$ pair forms an ordered 2D-compound. The same applies for each $O^{(11)} - O^{(10)} - O^{(11)}$ triplet. Together, they form an ordered 3D compound on a screw dislocation which is considered as 1D-defect. This 3D compound has no equivalent in the bulk since interaction between hydrogen atoms in the bulk are negligible. We have previously shown that the heterogeneous mean-field model, based on the definition of two sublattices for each line, corresponding to every other atom along the line, allows us to predict the temperature evolution of these ordered structures.

At higher temperatures, the empty interstitial sites and hydrogen atoms are randomly distributed forming a random solid solution. First, the composition deviates from stoichiometry for the triplet $O^{(11)} - O^{(10)} - O^{(11)}$ (see *figure 8 c and d*). While perfect order, at stoichiometric composition, is defined by a long-range order (LRO) parameter equals to 1, when the composition deviates from stoichiometry, (see *figure 8 c and d*), microstructures show that order can be described by short-range order (SRO):

- a H atom on a $O^{(10)}$ line is surrounded by two H atoms located on the two neighboring $O^{(11)}$ lines in the perpendicular direction of the Burgers vector due to the high attractive interaction V_P^2. The perpendicular inter-line order shows some defects (see *figure 8c*) with the presence of 2 H atoms instead of 3.
- a H atom is always surrounded by two empty sites on the same line (in the direction of the Burgers vector). This result may seem surprising, given that there are no interactions between the hydrogen atoms along the line. The intra-line order is the consequence of the perpendicular inter-line order and the strong diagonal repulsive interaction V_D^2.

Then, the composition deviates from stoichiometry for the $O^{(4)}$ pair (see *figure 8 f and g*). A strong perpendicular inter-line order is observed, as well as an intra-line order respectively due to V_P^1 and to V_D^1.

Note that microstructures of the other sectors of the dislocation are similar. There is never a perfectly ordered pair (or triplet) and the other two pairs empty simultaneously, which would be the signature of a phase separation.

The SRO can be characterized in Monte Carlo simulations by determining the Warren-Cowley parameter [57] :

$$\alpha_X = 1 - \frac{P^X_{H_i - E_j}}{1 - c_j} \quad (8)$$

where $X =$ intra, P or D for respectively intra-line, perpendicular inter-line or diagonal inter-line SRO parameters. $P^X_{H_i - E_j}$ is the probability to have heteroatomic bonds in nearest neighboring position in the X direction, i.e. to have an empty site in line j starting from a H atom in line i. For $X =$intra, $j = i$. c_j is the H concentration of line j. A random solid solution is characterized by $\alpha = 0$. For an ordered configuration $\alpha < 0$, whereas $\alpha > 0$ indicates a tendency to form homoatomic bonds. *Figure 8* depicts the SRO evolution as a function of the temperature.

As expected, the intra-line SRO parameter of the core lines is zero. In absence of interactions, the distribution of H atoms is a random solid solution. At low temperatures, the 3D compound is characterized by a perfect intra-line and diagonal order ($\alpha = -1$) on all octahedral lines, a perfect attraction in the perpendicular direction ($\alpha = 1$). Intra-line and diagonal inter-line order parameters increase to zero with increasing temperature. $T_{1/2}$ decay temperatures are found. On the other hand, the decrease in perpendicular inter-line order parameters occurs at higher temperatures than the associated $T_{1/2}$. Attraction between atoms is very strong, stronger than repulsion. Thus, the vanishing of the 3D compound at higher temperatures is not linked to the attractive term, as might have been expected from the iso-concentrations obtained in the heterogeneous mean field model.

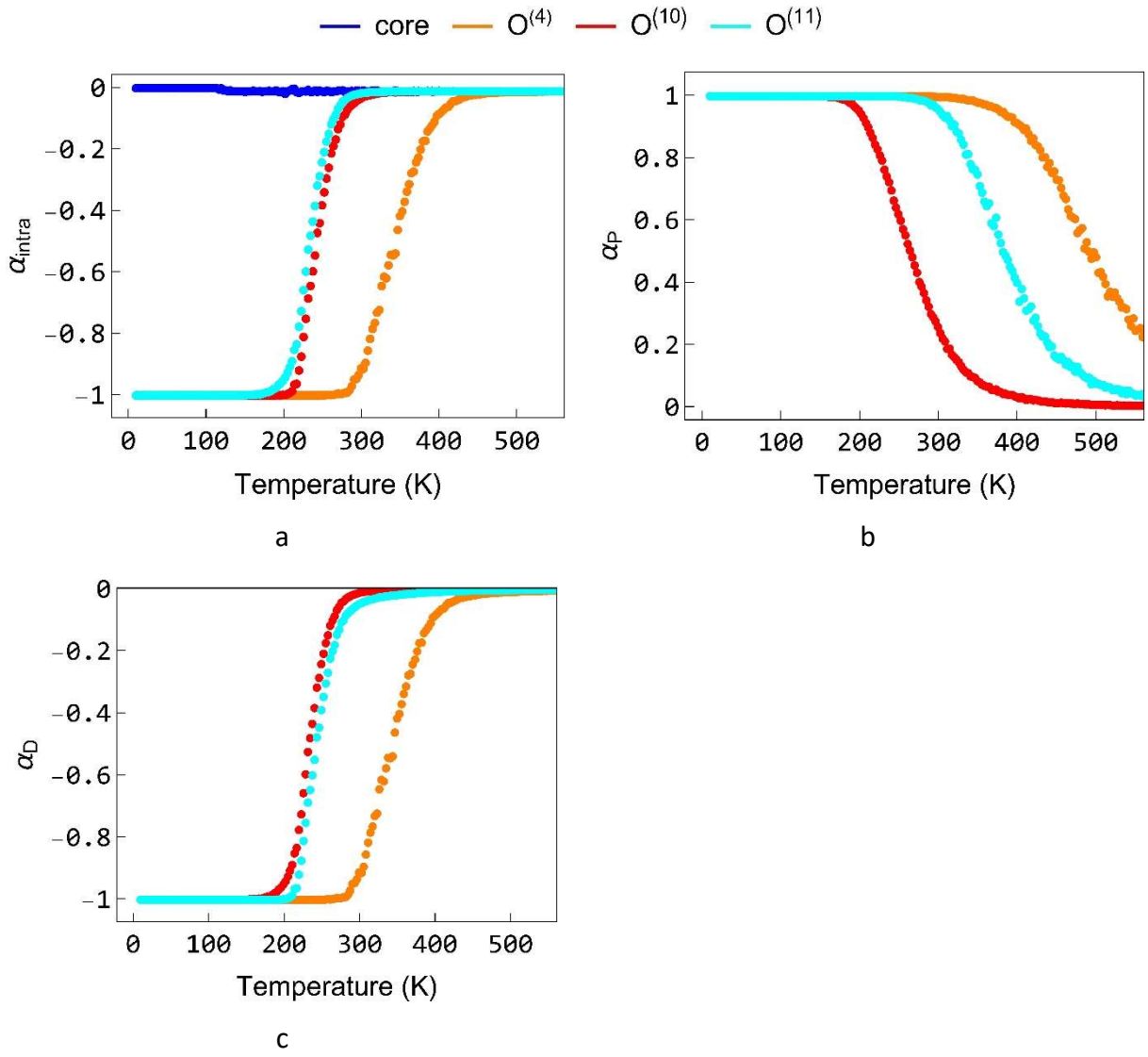

Fig. 9: SRO *evolution as a function of the temperature from Monte Carlo simulations in iron for* $c_{nom} = 100$ *appm. Intra-line SRO parameters (a), perpendicular inter-line SRO parameters (b) and diagonal inter-line SRO parameters (c).*

4. Discussion

Since there is no phase transition at 1D [56], it might be tempting to model the system with a homogeneous mean-field (see *section 2.3.2*). Although we have already shown that the heterogeneous mean-field is in good agreement with Monte Carlo simulations, we present below the iso-concentrations obtained from the homogeneous mean-field (see *figure 10*).

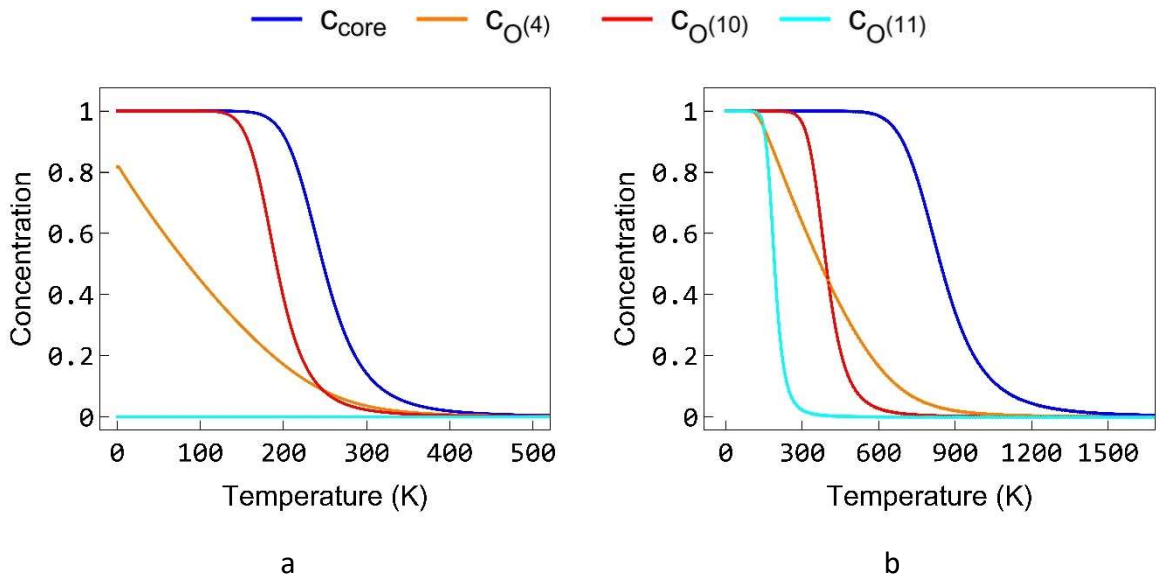

***Fig. 10**: Homogeneous Mean-Field iso-concentrations in iron (a) and tungsten (b) for* $c_{nom} = 100$ *appm.*

These results differ considerably from those obtained with the heterogeneous mean-field model (see *figure 3 and 5*) and Monte Carlo simulations (see *figure 7*).

For iron, at $T = 0$ K, core and $O^{(10)}$ lines are saturated, whereas the $O^{(11)}$ line is empty. The $O^{(4)}$ concentration is equal to about 0.82 (see *figure 3 and 5*), at 0 K the concentration of a line being 0 or 1. We previously showed [58] that this result is an artefact of the homogenous model. The observed value corresponds to the cancellation of the exponential argument in the fundamental segregation equation in the disordered state $\Delta E^{seg,0}_{O^{(4)}} + V^1_{eff}\, c_{O^{(4)}} = 0$ which results to $c_{O^{(4)}} = 0.826$. The curves of core and $O^{(10)}$ lines exhibit a plateau before decreasing and the $O^{(11)}$ line is empty throughout the temperature range. The decrease in concentration of the $O^{(4)}$ line begins at 0 K. The iso-concentration of the $O^{(4)}$ line is similar to that of a system with a tendency to order for temperatures above the critical order/disorder temperature. Since $\Delta E^{seg,0}_{O^{(11)}}$ is close to zero the segregation occurs preferentially on the other lines. The more hydrogen-rich the $O^{(10)}$ line, the more unfavorable the segregation on the $O^{(11)}$ line. Thus, at any temperature, the $O^{(11)}$ concentration is zero. Finally, whatever the temperature, the hierarchy of the enrichment is the following : $c_{core} > c_{O^{(10)}} > c_{O^{(4)}} > c_{O^{(11)}}$.

Iso-concentrations for tungsten are different from those for iron (see *figure 10 a and b*). All lines are fully saturated at 0 K. After a plateau, enrichment in hydrogen atoms decreases. For the $O^{(11)}$, $O^{(10)}$ and core lines, the hierarchy of the enrichment is linked solely to the segregation enthalpy in the dilute limit, since the effective interaction energies are all zero. The $O^{(11)}$ and $O^{(10)}$ lines are therefore independent whereas they are strongly coupled in MC simulations. Whatever the temperature, the core of the dislocation is richer than the octahedral lines.

To summarize, the homogeneous mean-field does not reproduce at all the Monte Carlo results. Remember that the Monte Carlo simulations are exact, given the underlying assumptions (lattice simulations), whereas the mean-field is based on the choice of a model and the Bragg-Williams approximation. Taking ordering into account modifies the main result of the homogeneous mean-field model, which shows that core sites are richer than octahedral sites. The heterogeneous mean-field model, which is a more elaborate statistical treatment, shows that the concentration of $O^{(4)}$ sites decreases at higher temperatures than the one of core sites in the case of iron, but not in the case of tungsten, in agreement with Monte Carlo simulations. Thus, the hierarchy of the decay temperatures, which depends on the competition between the segregation enthalpies in the dilute limit and the interaction energies, cannot be predicted without a detailed description of the dislocation.

5. Conclusions

Monte Carlo simulations of hydrogen segregation on screw dislocation in iron and tungsten have been carried out. The segregation profiles and microstructures have been determined at various temperatures. At low temperatures H atoms are ordered on octahedral sites and disordered in core sites forming a 3D hydride-like compound. The concentration of H atoms decreases with increasing temperature. For tungsten, the profile is monotonic, with a hydrogen enrichment that decreases with distance from the dislocation center. For iron, over a given temperature range, the profile is oscillating: $O^{(4)}$ sites are more enriched than core sites and $O^{(10)}$ and $O^{(11)}$ sites. The difference between the two metals is linked to the coupling between segregation and ordering. For both metals, the attractive interactions between H atoms in the direction perpendicular to the Burger vector direction is very strong and the

perpendicular order remains at high temperatures. Repulsive diagonal inter-line interactions lead to intra-line ordering, whereas there are no intra-line interactions. The profile evolution in temperature is well predicted with the heterogeneous MF formalism which considers the possibility of an ordered structure, whereas the homogeneous formalism gives incorrect profiles.

In summary, the approach presented here clearly demonstrates that the dislocation is enriched in hydrogen over an extended area around the dislocation core, forming a 3D hydride-like structure and that, in a given temperature range, the core of the dislocation can be less rich in hydrogen atoms than outer sites due to interactions between atoms that can lead to order. This is an important result for future studies about the mobility of screw dislocations.

Moreover, the agreement between heterogeneous MF and MC simulations is satisfactory, allowing the heterogeneous MF formalism to be used to study segregation in dislocations.

Declaration of Competing Interest

The authors declare that they have no known competing financial interests or personal relationships that could have appeared to influence the work reported in this paper.

Acknowledgments

We thank L. Ventelon and E. Clouet for giving us the opportunity to study the coupling between segregation and ordering on dislocations.

Appendix A

Since the heterogeneous mean-field model allows the presence of ordered structures on the octahedral lines, their phase diagrams can be determined by plotting the isotherms of the octahedral lines. In this appendix we only present the case of iron. *Figure A1a* shows the isotherms at a high temperature ($T = 1500$ K). At a temperature lower than the order/disorder critical temperature, the splitting of the isotherm of an octahedral line into two distinct α and β isotherms is the signature of the order-disorder transition. The transition is limited at a given temperature to a bulk concentration range c_{bulk}, characterized by the separation of the two sub-lattices isotherms, and to a line concentration range by the solubility limits (see *figure A1b*) that define the phase diagram (see *figure A3a*).

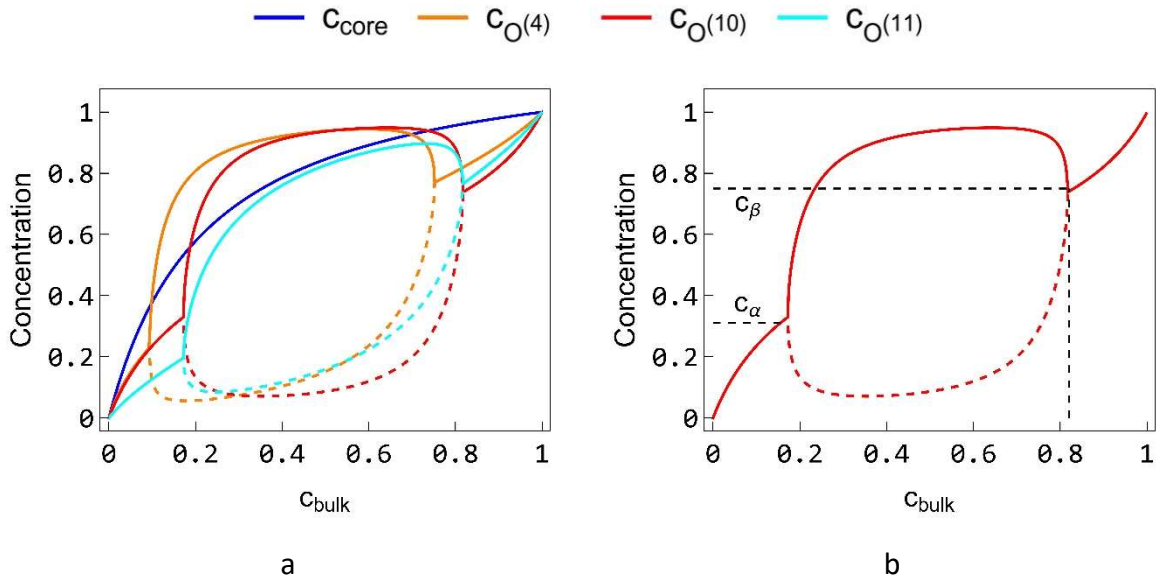

Fig. A1: *Heterogeneous Mean-Field isotherms with sub-lattices at $T = 1500$ K for iron (a). The solubility limits of the $O^{(10)}$ line are indicated by horizontal dashed lines on the $O^{(10)}$ isotherm (b). Sub-lattices* α *(hydrogen-rich): lines, sub-lattices* β *(hydrogen-poor): dashed lines.*

As the temperature decreases, the $O^{(4)}$ isotherm rich in H presents a van der Waals loop, indicating a first order perpendicular inter-line transition (see *figure A2a*). This demixtion-disorder transition is due to the attractive interaction between H atoms on a $O^{(4)}$ pair perpendicularly to the Burgers vector direction. The solubility limits are given by the rule of equal areas which ensures that the two phases, one rich and the other one poor in H atoms,

have the same free energy. The critical temperature is $T_c^{O^{(4)}} = -\frac{V_P^1}{4\,k_B} = 725$ K. The determination of the solubility limits as a function of the temperature leads to the phase diagram shown *figure A3b*.

At even lower temperatures, $O^{(10)}$ and $O^{(11)}$ isotherms are S-shaped (see *figure A2b*). These isotherms are coupled. The critical temperature is given by the equations [43]

$$\left.\frac{\partial c_{bulk}}{\partial c_{O^{(10)}}}\right|_{c_{O^{(10)}}^{crit}} = \left.\frac{\partial c_{bulk}}{\partial c_{O^{(11)}}}\right|_{c_{O^{(11)}}^{crit}} = 0 \text{ and } \left.\frac{\partial^2 c_{bulk}}{\partial c_{O^{(10)}}^2}\right|_{c_{O^{(10)}}^{crit}} = \left.\frac{\partial^2 c_{bulk}}{\partial c_{O^{(11)}}^2}\right|_{c_{O^{(11)}}^{crit}} = 0 \qquad \text{(A1)}$$

An analytical expression of the critical bilayer temperature is obtained only if $c_{O^{(10)}}^{crit} = c_{O^{(11)}}^{crit} = 0.5$, which is not the case here.

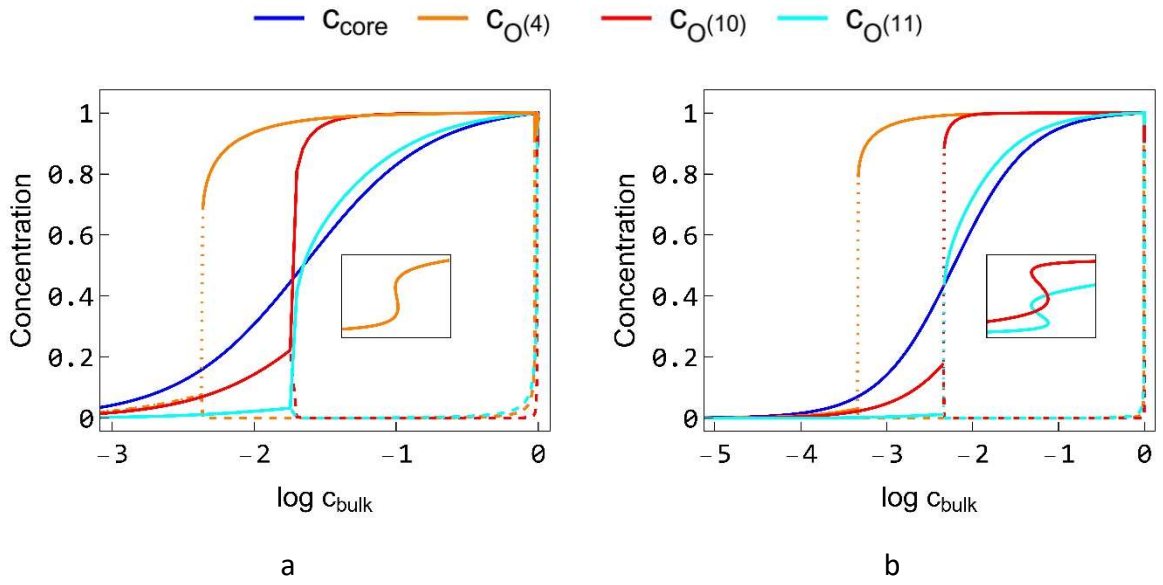

Fig. A2: *Heterogeneous Mean-Field isotherms with sub-lattices for iron at $T = 675$ K (a) and $T = 500$ K (b). Sub-lattices α (hydrogen-rich): lines, sub-lattices β (hydrogen-poor): dashed lines.*

The demixtion-disorder critical temperature for the $O^{(10)}$ and $O^{(11)}$ lines ($T_c^{O^{(10)}-O^{(11)}} \approx 600$ K) is lower than that for the $O^{(4)}$ line as shown on *figure A2*.

The order-disorder phase diagrams of O-lines $(\langle c_O \rangle, T)$ are almost symmetrical and the order-disorder critical temperatures for the three octahedral lines are almost the same and are close to 2000 K (see *figure A3a*). The demixtion-disorder phase diagram is perfectly symmetrical for line $O^{(4)}$ and highly asymmetrical for lines $O^{(10)}$ and $O^{(11)}$ (see *figure A3b*).

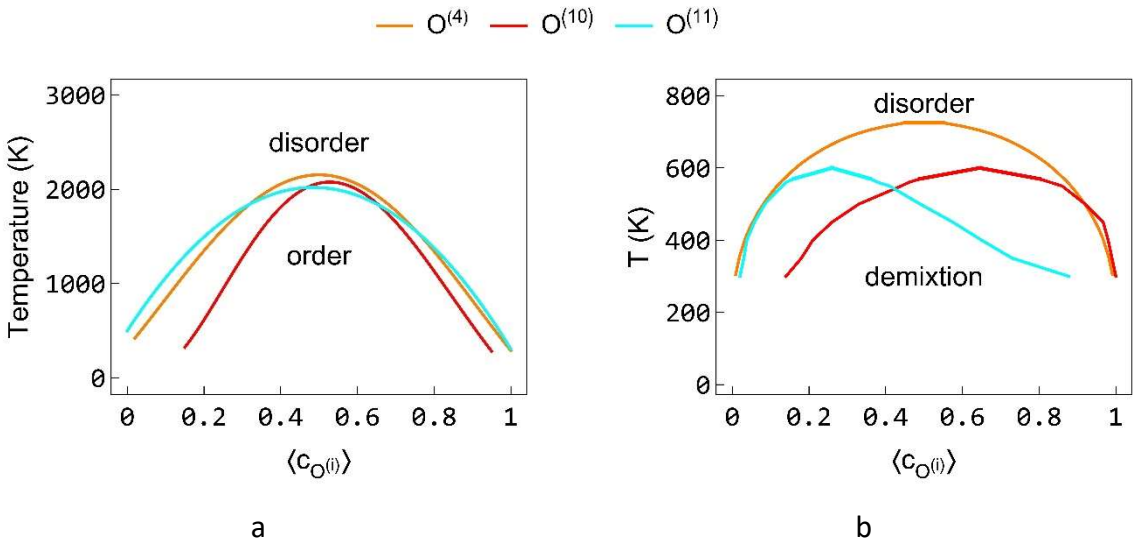

Fig. A3: *Heterogeneous Mean-Field order phase diagrams (a) and demixtion phase diagrams (b) of the octahedral lines for iron.*

These temperatures are high, and even if there is no phase transition as such in an exact statistical treatment, as in Monte Carlo simulations, this shows that a strong local order can exist over a relatively wide range of temperatures due to the segregation of hydrogen in the dislocations.

References

[1] W.H. Johnson, On some remarkable changes produced in iron and steel by the action of hydrogen and acids, Nature. 11 (1875) 393. https://doi.org/10.1038/011393a0.

[2] M. Aucouturier, Grain Boundary Segregations and Hydrogen Embrittlement., J. Phys. (Paris), Colloq. 43 (1982) 175–186. https://doi.org/10.1051/jphyscol:1982617.

[3] Z. Guo, M. Zhao, C. Li, S. Chen, L. Rong, Mechanism of hydrogen embrittlement in a gamma-prime phase strengthened Fe-Ni based austenitic alloy, Mater. Sci. Eng. A. 555 (2012) 77–84. https://doi.org/10.1016/j.msea.2012.06.036.

[4] F.F. Dear, G.C.G. Skinner, Mechanisms of hydrogen embrittlement in steels: Discussion, Philos. Trans. R. Soc. A Math. Phys. Eng. Sci. 375 (2017). https://doi.org/10.1098/rsta.2017.0032.

[5] J.S. Wang, The thermodynamics aspects of hydrogen induced embrittlement, Eng. Fract. Mech. 68 (2001) 647–669. https://doi.org/10.1016/S0013-7944(00)00120-X.

[6] I.M. Robertson, P. Sofronis, A. Nagao, M.L. Martin, S. Wang, D.W. Gross, K.E. Nygren, Hydrogen Embrittlement Understood, Metall. Mater. Trans. B. 46 (2015) 1085–1103. https://doi.org/10.1007/s11663-015-0325-y.

[7] J. Song, W.A. Curtin, Atomic mechanism and prediction of hydrogen embrittlement in iron, Nat. Mater. 12 (2013) 145–151. https://doi.org/10.1038/nmat3479.

[8] I.M. Robertson, H.K. Birnbaum, An HVEM study of hydrogen effects on the deformation and fracture of nickel, Acta Metall. 34 (1986) 353–366. https://doi.org/10.1016/0001-6160(86)90071-4.

[9] D.S. Shih, I.M. Robertson, H.K. Birnbaum, Hydrogen embrittlement of α titanium: In situ tem studies, Acta Metall. 36 (1988) 111–124. https://doi.org/10.1016/0001-6160(88)90032-6.

[10] L. Huang, D. Chen, D. Xie, S. Li, Y. Zhang, T. Zhu, D. Raabe, E. Ma, J. Li, Z. Shan, Quantitative tests revealing hydrogen-enhanced dislocation motion in α-iron, Nat. Mater. 22 (2023) 710–716. https://doi.org/10.1038/s41563-023-01537-w.

[11] T. Tabata, H.K. Birnbaum, Direct observations of the effect of hydrogen on the

behavior of dislocations in iron, Scr. Metall. 17 (1983) 947–950. https://doi.org/10.1016/0036-9748(83)90268-5.

[12] R. Matsumoto, S.T. Oyinbo, M. Vijendran, S. Taketomi, Hydrogen Effect on the Mobility of Edge Dislocation in α-Iron: A Long-Timescale Molecular Dynamics Simulation, ISIJ Int. 62 (2022) ISIJINT-2022-311. https://doi.org/10.2355/isijinternational.ISIJINT-2022-311.

[13] J. Song, W.A. Curtin, Mechanisms of hydrogen-enhanced localized plasticity: An atomistic study using α-Fe as a model system, Acta Mater. 68 (2014) 61–69. https://doi.org/10.1016/j.actamat.2014.01.008.

[14] H.H. Pham, T. Cagin, Fundamental Study of Hydrogen Segregation at Vacancy and Grain Boundary in Palladium, (2015). http://arxiv.org/abs/1506.00302.

[15] P. Ekborg-Tanner, P. Erhart, Hydrogen-Driven Surface Segregation in Pd Alloys from Atomic-Scale Simulations, J. Phys. Chem. C. 125 (2021) 17248–17260. https://doi.org/10.1021/acs.jpcc.1c00575.

[16] J.I. Postma, A. Ferrari, A.J. Böttger, Monte Carlo simulations of surface segregation to discover new hydrogen separation membranes, Int. J. Hydrogen Energy. 48 (2023) 2221–2230. https://doi.org/10.1016/j.ijhydene.2022.10.057.

[17] K. Ito, Y. Tanaka, K. Tsutsui, H. Sawada, Analysis of grain-boundary segregation of hydrogen in bcc-Fe polycrystals via a nano-polycrystalline grain-boundary model, Comput. Mater. Sci. 225 (2023) 112196. https://doi.org/10.1016/j.commatsci.2023.112196.

[18] Y. Zheng, P. Yu, K. Zhang, M. Wen, J. Zheng, C. Zhou, L. Zhang, Coupling effect of grain boundary and hydrogen segregation on dislocation nucleation in bi-crystal nickel, Int. J. Hydrogen Energy. 45 (2020) 20021–20031. https://doi.org/10.1016/j.ijhydene.2020.04.291.

[19] C.M. Lousada, P.A. Korzhavyi, Hydrogen at symmetric tilt grain boundaries in aluminum: segregation energies and structural features, Sci. Rep. 12 (2022) 1–13. https://doi.org/10.1038/s41598-022-23535-9.

[20] X.J. Shen, D. Tanguy, D. Connétable, Atomistic modelling of hydrogen segregation to

the Σ9{2 2 1}[1 1 0] symmetric tilt grain boundary in Al, Philos. Mag. 94 (2014) 2247–2261. https://doi.org/10.1080/14786435.2014.910333.

[21] S. Jothi, T.N. Croft, L. Wright, A. Turnbull, S.G.R. Brown, Multi-phase modelling of intergranular hydrogen segregation/trapping for hydrogen embrittlement, Int. J. Hydrogen Energy. 40 (2015) 15105–15123. https://doi.org/10.1016/j.ijhydene.2015.08.093.

[22] D. Connétable, Y. Wang, D. Tanguy, Segregation of hydrogen to defects in nickel using first-principles calculations: The case of self-interstitials and cavities, J. Alloys Compd. 614 (2014) 211–220. https://doi.org/10.1016/j.jallcom.2014.05.094.

[23] C.J. O'Brien, S.M. Foiles, Hydrogen segregation to inclined twin grain boundaries in nickel, Philos. Mag. 96 (2016) 2808–2828. https://doi.org/10.1080/14786435.2016.1217094.

[24] C. Nowak, X.W. Zhou, An interplay between a hydrogen atmosphere and dislocation characteristics in BCC Fe from time-averaged molecular dynamics, Phys. Chem. Chem. Phys. (2023). https://doi.org/10.1039/d2cp05024b.

[25] Y. Wang, X. Wang, X. Wu, Q. Li, C. Li, G. Shu, B. Xu, W. Liu, Hydrogen distribution induced screw dislocation core spreading in tungsten, J. Nucl. Mater. 523 (2019) 71–79. https://doi.org/10.1016/j.jnucmat.2019.05.038.

[26] R. Kirchheim, A. Pundt, Segregation of hydrogen at dislocations, 11th Int. Conf. Fract. 2005, ICF11. 5 (2005) 3324–3329.

[27] S.H. Bak, S.S. Kim, D.B. Lee, Effect of hydrogen on dislocation structure and strain-induced martensite transformation in 316L stainless steel, RSC Adv. 7 (2017) 27840–27845. https://doi.org/10.1039/C7RA01053B.

[28] P. Grigorev, T.D. Swinburne, J.R. Kermode, Hybrid quantum/classical study of hydrogen-decorated screw dislocations in tungsten: Ultrafast pipe diffusion, core reconstruction, and effects on glide mechanism, Phys. Rev. Mater. 4 (2020) 023601. https://doi.org/10.1103/PhysRevMaterials.4.023601.

[29] P.P.P.O. Borges, E. Clouet, L. Ventelon, Ab initio investigation of the screw dislocation-hydrogen interaction in bcc tungsten and iron, Acta Mater. 234 (2022) 118048.

https://doi.org/10.1016/j.actamat.2022.118048.

[30] Y.-H. Li, H.-B. Zhou, F. Gao, G. Lu, G.-H. Lu, F. Liu, Hydrogen induced dislocation core reconstruction in bcc tungsten, Acta Mater. 226 (2022) 117622. https://doi.org/10.1016/j.actamat.2022.117622.

[31] Y. Zheng, P. Yu, L. Zhang, Atomistic Study of the Interaction Nature of H-Dislocation and the Validity of Elasticity in Bcc Iron, Metals (Basel). 13 (2023) 1267. https://doi.org/10.3390/met13071267.

[32] G. Hachet, J. Li, A.M. Hallil, A. Metsue, A. Oudriss, J. Bouhattate, X. Feaugas, A multi-scale analysis of the different interactions between defects and hydrogen: A review on the contribution of the elastic fields, Eng. Fract. Mech. 218 (2019) 106621. https://doi.org/10.1016/j.engfracmech.2019.106621.

[33] Y. Tang, J.A. El-Awady, Atomistic simulations of the interactions of hydrogen with dislocations in fcc metals, Phys. Rev. B. 86 (2012) 174102. https://doi.org/10.1103/PhysRevB.86.174102.

[34] A. Ramasubramaniam, M. Itakura, E.A. Carter, Interatomic potentials for hydrogen in α –iron based on density functional theory, Phys. Rev. B. 79 (2009) 174101. https://doi.org/10.1103/PhysRevB.79.174101.

[35] P. Yu, Y. Cui, G. Zhu, Y. Shen, M. Wen, The key role played by dislocation core radius and energy in hydrogen interaction with dislocations, Acta Mater. 185 (2020) 518–527. https://doi.org/10.1016/j.actamat.2019.12.033.

[36] A. Drexler, S. He, R. Pippan, L. Romaner, V.I. Razumovskiy, W. Ecker, Hydrogen segregation near a crack tip in nickel, Scr. Mater. 194 (2021) 113697. https://doi.org/10.1016/j.scriptamat.2020.113697.

[37] M. Itakura, H. Kaburaki, M. Yamaguchi, T. Okita, The effect of hydrogen atoms on the screw dislocation mobility in bcc iron: A first-principles study, Acta Mater. 61 (2013) 6857–6867. https://doi.org/10.1016/j.actamat.2013.07.064.

[38] A. Hizi, A. Front, M. Said, F. Berthier, G. Tréglia, C. Mottet, Tight-binding Ising modeling of the interplay between bulk ordering and surface segregation in Pt-Ag nanoalloys, Surf. Sci. 700 (2020) 121626. https://doi.org/10.1016/j.susc.2020.121626.

[39] M. Schmid, P. Varga, Segregation and surface chemical ordering − an experimental view on the atomic scale, in: Chem. Phys. Solid Surfaces, Elsevier B.V., 2002: pp. 118–151. https://doi.org/10.1016/S1571-0785(02)80091-8.

[40] G. Tréglia, B. Legrand, F. Ducastelle, A. Saúl, C. Gallis, I. Meunier, C. Mottet, A. Senhaji, Alloy surfaces: segregation, reconstruction and phase transitions, Comput. Mater. Sci. 15 (1999) 196–235. https://doi.org/10.1016/S0927-0256(99)00004-X.

[41] D. Luan, H. Jiang, Theoretical study of surface segregation and ordering in Ni-based bimetallic surface alloys, J. Chem. Phys. 154 (2021) 074702. https://doi.org/10.1063/5.0037913.

[42] R. Tétot, F. Berthier, J. Creuze, I. Meunier, G. Tréglia, B. Legrand, Cu-Ag (111) Polymorphism Induced by Segregation and Advacancies, Phys. Rev. Lett. 91 (2003) 176103. https://doi.org/10.1103/PhysRevLett.91.176103.

[43] F. Berthier, J. Creuze, R. Tétot, B. Legrand, Multilayer properties of superficial and intergranular segregation isotherms: A mean-field approach, Phys. Rev. B. 65 (2002) 195413. https://doi.org/10.1103/PhysRevB.65.195413.

[44] J.D. Rittner, D.N. Seidman, Solute-atom segregation to 〈110〉 symmetric tilt grain boundaries, Acta Mater. 45 (1997) 3191–3202. https://doi.org/10.1016/S1359-6454(97)00002-5.

[45] A. Lopes, G. Tréglia, C. Mottet, B. Legrand, Ordering and surface segregation in Co1-cPtc nanoparticles: A theoretical study from surface alloys to nanoalloys, Phys. Rev. B. 91 (2015) 035407. https://doi.org/10.1103/PhysRevB.91.035407.

[46] J. Creuze, F. Berthier, R. Tétot, B. Legrand, Intergranular segregation and ordering effect: A mixed Monte Carlo mean-field approach, Phys. Rev. B. 62 (2000) 2813–2824. https://doi.org/10.1103/PhysRevB.62.2813.

[47] J. Creuze, F. Berthier, R. Tétot, B. Legrand, D. Tanguy, Segregation and 2D-Compound in a Grain Boundary: An Exotic Behaviour, Mater. Sci. Forum. 294–296 (1998) 423–426. https://doi.org/10.4028/www.scientific.net/MSF.294-296.423.

[48] A. Detor, C. Schuh, Grain boundary segregation, chemical ordering and stability of nanocrystalline alloys: Atomistic computer simulations in the Ni–W system, Acta

Mater. 55 (2007) 4221–4232. https://doi.org/10.1016/j.actamat.2007.03.024.

[49] Binder Kurt, Applications of the Monte Carlo Method in Statistical Physics, Springer Berlin Heidelberg, Berlin, Heidelberg, 1984. https://doi.org/10.1007/978-3-642-96788-7.

[50] Binder Kurt, Monte Carlo Methods in Statistical Physics, Springer Berlin Heidelberg, Berlin, Heidelberg, 1986. https://doi.org/10.1007/978-3-642-82803-4.

[51] Allen M.P., Tildesley D.J., Computer Simulation of Liquids, Oxford University, New York, 1987.

[52] N. Metropolis, A.W. Rosenbluth, M.N. Rosenbluth, A.H. Teller, E. Teller, Equation of State Calculations by Fast Computing Machines, J. Chem. Phys. 21 (1953) 1087–1092. https://doi.org/10.1063/1.1699114.

[53] J. Tersoff, Oscillatory segregation at a metal alloy surface: Relation to ordered bulk phases, Phys. Rev. B. 42 (1990) 10965–10968. https://doi.org/10.1103/PhysRevB.42.10965.

[54] K.R. Mecke, S. Dietrich, Segregation profiles in Cu3Au above the order-disorder transition, Phys. Rev. B. 52 (1995) 2107–2116. https://doi.org/10.1103/PhysRevB.52.2107.

[55] J. Creuze, F. Berthier, B. Legrand, Segregation and Phase Transitions in Reduced Dimension: From Bulk to Clusters via Surfaces, in: 2012: pp. 227–257. https://doi.org/10.1007/978-1-4471-4014-6_7.

[56] F. Ducastelle., Order and Phase Stability in Alloys., (Cohesion Struct. Vol. 3). North-Holland/Elsevier Sci. Publ. Amsterdam. (1991). https://onlinelibrary.wiley.com/doi/10.1002/crat.2170270624.

[57] B. E. Warren, X-ray Diffraction, Dover, New-York, 1990.

[58] F. Berthier, B. Legrand, Influence of ordering phenomena on carbon segregation in tungsten screw dislocation, Acta Mater. 245 (2023) 118610. https://doi.org/10.1016/j.actamat.2022.118610.